Dissimilar linear friction welding of selective laser melted Inconel 718 to forged Ni-based superalloy AD730TM: evolution of strengthening phases

Seyedmohammad Tabaie, Farhad Rezai-Aria, Bertrand C.D. Flipo, Mohammad Jahazi

Dissimilar linear friction welding of selective laser melted Inconel 718 to forged Ni-based superalloy AD730^{TM}: Evolution of strengthening phases

Seyedmohammad Tabaie [a], Farhad Rézaï-Aria [b], Bertrand C.D. Flipo [c], Mohammad Jahazi [a,*]

[a] Department of Mechanical Engineering, École de Technologie Supérieure (ÉTS), H3C 1K3 Montreal, QC, Canada
[b] Institut Clément Ader (ICA), Université de Toulouse, CNRS, IMT Mines Albi, INSA, UPS, ISAE, Campus Jarlard, 81013 Albi, France
[c] TWI Ltd, Granta Park, Great Abington, Cambridge CB21 6AL, United Kingdom

Keywords:
Additive manufacturing
Linear friction welding
Ni-based superalloy
Precipitation
Microhardness
Strengthening mechanisms

A B S T R A C T

The continuous growth in the manufacture of aerospace components such as blisks has led to an increase in the application of different hybrid materials fabricating methods, and thus the requirements for joining and strengthening of dissimilar welds. According to this goal, selective laser melted (SLM) Inconel 718 was joined with forged AD730^{TM} Nickel-based superalloy through linear friction welding (LFW) in this study. Microstructure variation, specifically with respect to secondary phases precipitation was investigated. The microhardness and strengthening mechanisms of the weldment were also studied. The precipitation (volume fraction and size of particles) at different regions of both sides of the weld line was characterized. Close to the weld line, the dissolution of γ'/γ'' and Laves phases and grain refinement occurred which reveals the effects of both compression strain and high temperature on recrystallization and high degree of elemental diffusion in the weld zone (WZ). It is shown that the size, volume fraction, and shape of secondary phases increased and changed (from spherical to long-striped for Laves particles) as we went from the WZ toward the base metal. However, the measured microhardness indicated that the strength of AD730^{TM} alloy depends significantly on the grain size, while strength in SLM Inconel 718 was dominated by shape (or size) and the presence of secondary phases (γ'/γ'' and Laves).

1. Introduction

The demand for joining different components by welding dissimilar materials is growing continuously for the aerospace industry. Among the various techniques, friction based solid-state welding processes are well suited for joining dissimilar alloys as they do not suffer from weld shrinkage and cracking which are very common in fusion based techniques [1,2]. The welding can be realized by rotating or linear movement of one part against another part that is maintained stable in a static position while a compressive load is exerted. During linear friction welding (LFW), a reciprocating movement and a normal pressure are, imposed on the two surfaces to be joined. Due to the frictional force and accumulated micro-plastic mechanical strain under the contact surface, the heat generated increases the temperature at contact surfaces. When the temperature becomes high enough to decrease the plastic flow limit and increase the ductility of the two materials, a forging pressure is applied in the last step to weld them together. Hence, this technique can be suitable for assembling dissimilar materials [1,3]. This thermomechanical deformation process imposes three different zones away from the weld interface: weld zone (WZ), where the highest deformation and temperature are achieved, the thermomechanical affected zone (TMAZ) where material experiences small scale thermo-plastic yielding, and the heat-affected zone (HAZ) where the material is only affected by the heat of welding, respectively. Beyond the HAZ, the base metal (BM) is remained free of thermomechanically-induced changes [1,3].

Selective laser melting (SLM) as a laser powder bed fusion (LPBF) method is being developed as an economically viable technology for fabricating Ni-based superalloy with the complex geometries in aerospace industries and also as an advanced technique for component repair. Gas turbine blades are known for their complex geometries and high time to market delay [4-7]. To be able to fully utilize the SLM process as a commercial production process, welding of its components with complex geometries will be an issue [8,9]. Welding is the main joining method for metallic materials and thus, a combination of LFW and SLM which are

* Corresponding author.
E-mail address: Mohammmad.Jahazi@etsmtl.ca (M. Jahazi).

two advanced techniques could open new possibilities for the gas turbine industry as well as for other high value-added industries. The behavior of SLM-manufactured material during welding is an important concern that needs to be investigated.

The Ni-based superalloys are used extensively for the aerospace engine, gas turbines, and nuclear applications due to their excellent mechanical properties at high temperatures. These alloys are mainly strengthened by precipitation mechanisms, either by γ', Ni_3(Al, Ti) in AD730^{TM}, Waspaloy, and U720Li or by a combination of γ'' (Ni_3Nb) and γ' (Ni_3(Al, Ti)) in Inconel 718 (IN718) [10,11]. In addition, alloying elements such as Co, Fe, Cr, Ti, Al, Nb, Mo, W, and Ta provide an extra strengthening of the gamma phase matrix by solid solution mechanism (σ_{ss}) [12–16].

To date, some similar LFW of Ni-superalloys such as IN718 [17], AD730^{TM} [18], Waspaloy [19], and GH4169 alloy [20] have been successfully joined by LFW, while few works have been reported for LFW of dissimilar Ni-based superalloys. Compared to similar materials welding, dissimilar welds are generally more difficult to be successfully achieved due to the different thermomechanical properties of the two base materials [21–26]. LFW conditions, such as friction and forge pressures, strain, strain rate, temperature, heating and cooling rates, could affect the microstructure of materials during the welding process at different zones. Karadge et al.[27] reported the specific difficulties encountered when welding a single-crystal superalloy CMSX4 to polycrystalline a Ni-based superalloy RR1000 having extremely different microstructures. The authors also briefly mentioned the variation of microstructure across the weld line, but no mechanical properties of the weldment were reported. Huang et al. [26] applied the inertia friction welding (IFW) method to weld 720Li superalloy to IN718 alloy. Their results showed weld free of micropores and microcracks with no significant chemical migration of alloy elements across the weld line. The authors observed a significant variation of the microstructure, which resulted in a partial or full dissolution of secondary precipitates (γ', γ'', and δ phases) in the region close to weld because of drastic thermal-mechanical solicitation experiencing by sever high plastic deformation loading. It has been reported [1,21,23,28] that for some IFW or LFW of Ni-based superalloys, the WZ is free of secondary precipitate phases. Jokisch et al. [29] reported that the dissolution of Laves, γ', and γ'' phases have occurred near the weld line region because the temperature reached in the range of the homogenization and forging temperatures. Ye et al. [21] reported the dissolution of γ' and γ'' close to the weld line on both sides of a dissimilar LFW of IN713LC and IN718. However, the re-precipitation of γ' was only observed in IN713LC in as-weld state. All these material evaluations and changes could have a huge impact on the mechanical properties of the weldment. However, the influence of the microstructure on plastic deformation behavior of the superalloys and consequently strengthening mechanisms need to be assessed.

It should be noted that it is not clear whether liquation of second phases, which often induces microcracking during fusion welding of Ni-based superalloys, also takes place in LFW. Liquation and liquation cracking have been observed by Smith et al. [30] and Vishwakarma et al. [31] for LFW of as-serviced IN718 and Allvac 718 Plus, respectively. In addition, Raza et al. [32,33] reported liquation cracks in the HAZ microstructure of gas tungsten arc-welded SLM IN718. However, for LFW of AD730^{TM} [34], Waspaloy [19], and dissimilar IN713LC-IN718 [21] liquation have not been reported. Besides, no liquation was observed by Jokisch et al. [29] for dissimilar laser welding of SLM IN718 and IN625; however, both alloys have almost the same mechanical properties at high temperatures. In contrast, dissimilar welding of alloys with significant differences in their mechanical properties and strengthening mechanisms increases the risk for liquation and therefore needs to be investigated.

In the present study, a detailed microstructural analysis of LFW joints of two dissimilar Ni-based superalloys SLM IN718 and forged AD730^{TM} is carried out, with a particular focus on the evolution of the strengthening phases and liquation. Microstructural evolutions, such as changes in volume fraction and size of precipitates in different zones and liquation are correlated with the evolution of microhardness, which could be useful to assess their impacts on strengthening mechanisms and mechanical properties of the joint. The obtained results will help in designing pre- and post-weld procedures and controlling the mechanical properties of weldments of dissimilar additively manufactured components to the conventional polycrystalline parts produced by the dissimilar welding of additively manufactured components to the alloy is fabricated by traditional method.

2. Experimental procedures

The forged AD730^{TM} alloy was provided by Aubert & Duval. The alloy was vacuum induction melted (VIM) and then refined by vacuum arc remelting (VAR) in the form of an ingot that was then radially forged into a bar-round billet. The billet was cut into disks. The as-received disk of AD730^{TM} alloy is first solutionized (at 1080 °C for 4 h) and then wire electro-discharge machined (EDM) to produce rectangular coupons (L (length)=26 mm, W (width)=13 mm, and H (height)= 37 mm) for LFW. The initial average grain size of the microstructure was 41.36 ± 9.14 µm with a γ' volume fraction of 40% (the total volume fraction of all types of γ'). Its chemical composition is provided in Table 1.

Similar rectangular coupons (L = 26 mm, W = 13 mm, and H = 40 mm) of IN718 superalloy were selective laser melted by an SLM-125HL machine at IMT-Mines Albi, France, and used in as-fabricated conditions for LFW. Spherical shaped powders with a particle size distribution between 15 and 50 μm were used for SLM processing. The building direction was along with the Z-direction perpendicular to the fabrication platform. Laser beam scanning orientation in building direction was rotated successively for 67° in each layer to reduce microstructural anisotropy. Post-fabrication chemical analysis was carried out by Atomic Emission Spectroscopy (AES). The results are reported in Table 1 and are based on an average of five measurements.

The FW34-E20 LFW machine at TWI, Cambridge, UK was used for LFW of coupons from these dissimilar alloys. Fig. 1 shows a schematic of LFW processing. The pressure (both friction and forge) was applied perpendicular to the cross-section defined by the length and the width (i.e. area of L-W) of coupons. The direction of oscillations during LFW, was perpendicular to the SLM building direction of as-SLM-IN718 sample (on the top part of the as-SLM sample) and parallel in-plane of the contact the surface in contact with the AD730^{TM}. In order to remove any oxidation and contamination, the contact surfaces were grinded by SiC paper up to 800 grade and cleaned out by acetone. Details of the LFW processing conditions are provided in Table 2 and Fig. 1. Axial shortening or height reduction after LFW is a reliable indication of the combined effects of LFW process parameters such as frequency (f), oscillation amplitude (a), friction and forge pressures, and the welding time, which all affect the quality of the joint.

Following the welding the sample was EDM cross-sectioned perpendicular to the welding line in the center of the sample along the longitudinal axis (the red rectangular area in Fig. 1). The cross-sectioned samples were polished by standard metallographic preparation techniques and etched by waterless Kalling and Marble solutions for microstructure investigations. A LEXT OLS4100 laser confocal microscope was used for light microscopy (OM) investigation. Scanning electron microscopy (SEM) examinations were carried out on a Hitachi TM3000 tabletop SEM as well as a Hitachi SU-8230 Field Emission SEM equipped with a Bruker Electron

Table 1
Chemical compositions of bulk of alloys (wt.%). Chemical potentials for driving the elements by diffusion near the weld line are indicated by positive sign that means element diffusion from AD730™ to SLM IN718 and negative sign in the opposite direction.

Alloy	Elements												
	Ni	Fe	Cr	Co	Mo	W	Al	Ti	Nb	B	C	Zr	Si
AD730-Forged	Bal.	4	15.7	8.5	3.1	2.7	2.25	3.4	1.1	0.01	0.015	0.03	–
IN718-SLM	Bal.	15.7	20.54	0.1	3.13	–	0.34	1.17	5.1	0.002	0.04	0.018	0.01
AD730-IN718	+5.35	−11.7	−4.84	+8.4	−0.03	+2.7	+1.91	+2.23	−4	No significant changes			

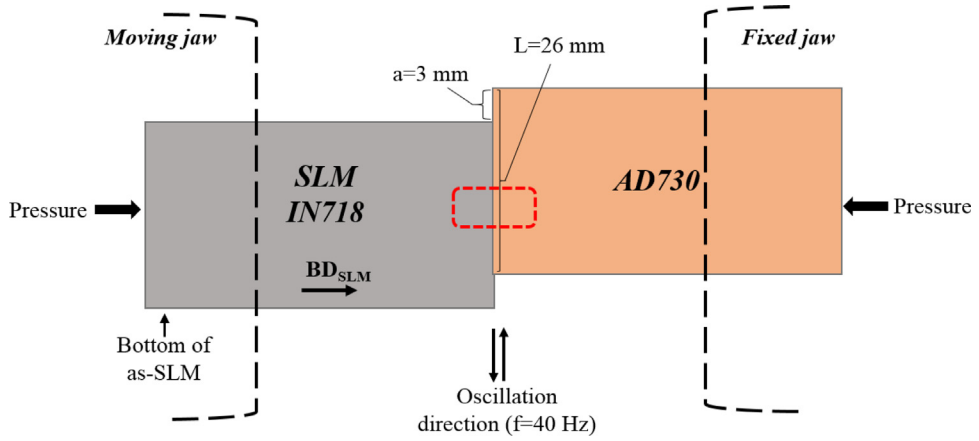

Fig. 1. Schematic presentation of LFW process for dissimilar Ni-based superalloys of AD730™ and as-SLM IN718 and H-SLM IN718 alloys. The building direction (BD) in the SLM sample is shown with black arrow. The dashed rectangular area is EDMed for the microstructural analysis.

Table 2
LFW processing parameters in the current study.

LFW Sample	a (mm)	f (Hz)	Friction pressure (MPa)	Time of process (s)	Forge pressure (MPa)	Heat input (W m^{-2})	Axial shortening (mm)
SLM IN718 & AD730	3	40	228	15.4	340	6.74×10^{7}	3.3

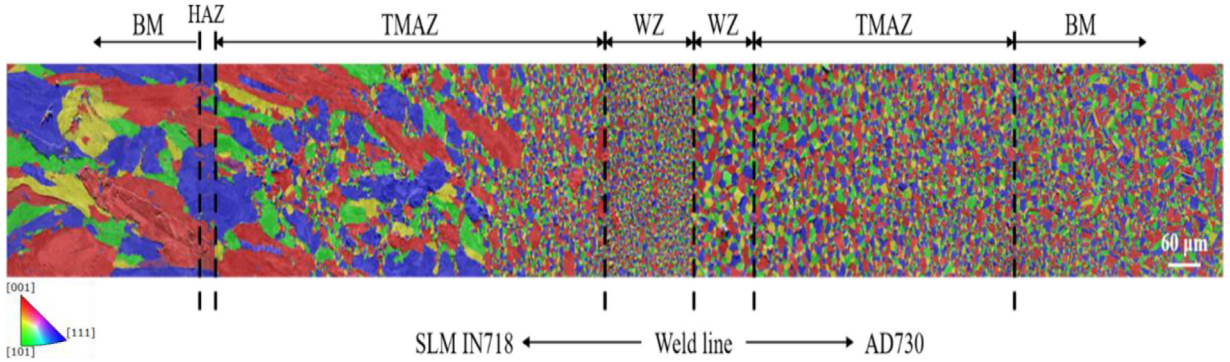

Fig. 2. EBSD grain map from different zones after LFW on both sides. The HAZ on the side of AD730™ was not observed.

Backscatter Diffraction (EBSD) and Quad Energy Dispersive Spectroscopy (EDS) detectors.

The particle size and volume fractions (V_f) of all precipitates (γ', γ", and Laves) were analyzed and measured by digitized microscopic images using ImageJ analysis software. The size and/or volume fraction are an average of 3–5 measurements. In each case, area measurements were carried out on more than 50 precipitates.

The specimen for EBSD examinations was prepared on a Buehler VibroMet™ polisher using a 0.05 μm colloidal silica suspension. Then, the specimen was ion milled by an Ion Beam Milling System (IM 4000Plus, Hitachi). Grain size variations in each alloy in the weld region, was measured with a step size of 0.47 μm in EBSD grain mapping (Fig. 2). The step size was changed between 90 nm and 0.47 μm because of the grains size variations or recrystallization taking place in LFW. The step size was 90 nm in regions having finer grain (close to the weld line or the WZ). It was changed to 0.47 μm in non-recrystallized regions with coarse grains (TMAZ, HAZ, and BM). At least 300 grains were characterized for evaluating the average grains size at each zone of each alloy (see [35] and Section 3.4, hereafter). The EBSD data were analyzed using Esprit software developed by Bruker for grains size distributions and EDS analysis.

The microhardness (HV) was measured over approximately 3 mm distance from the weld line to the BM (load of 200 g and a dwell time of 15 s) by a Future-Tech Vickers instrument was used to measure the microhardness (HV) in order to evaluate the weld strength variations on the across-sectioned the weld regions LFWed in both superalloys. Measurements were done over a distance of approximately 3 mm from the weld interface to the BM.

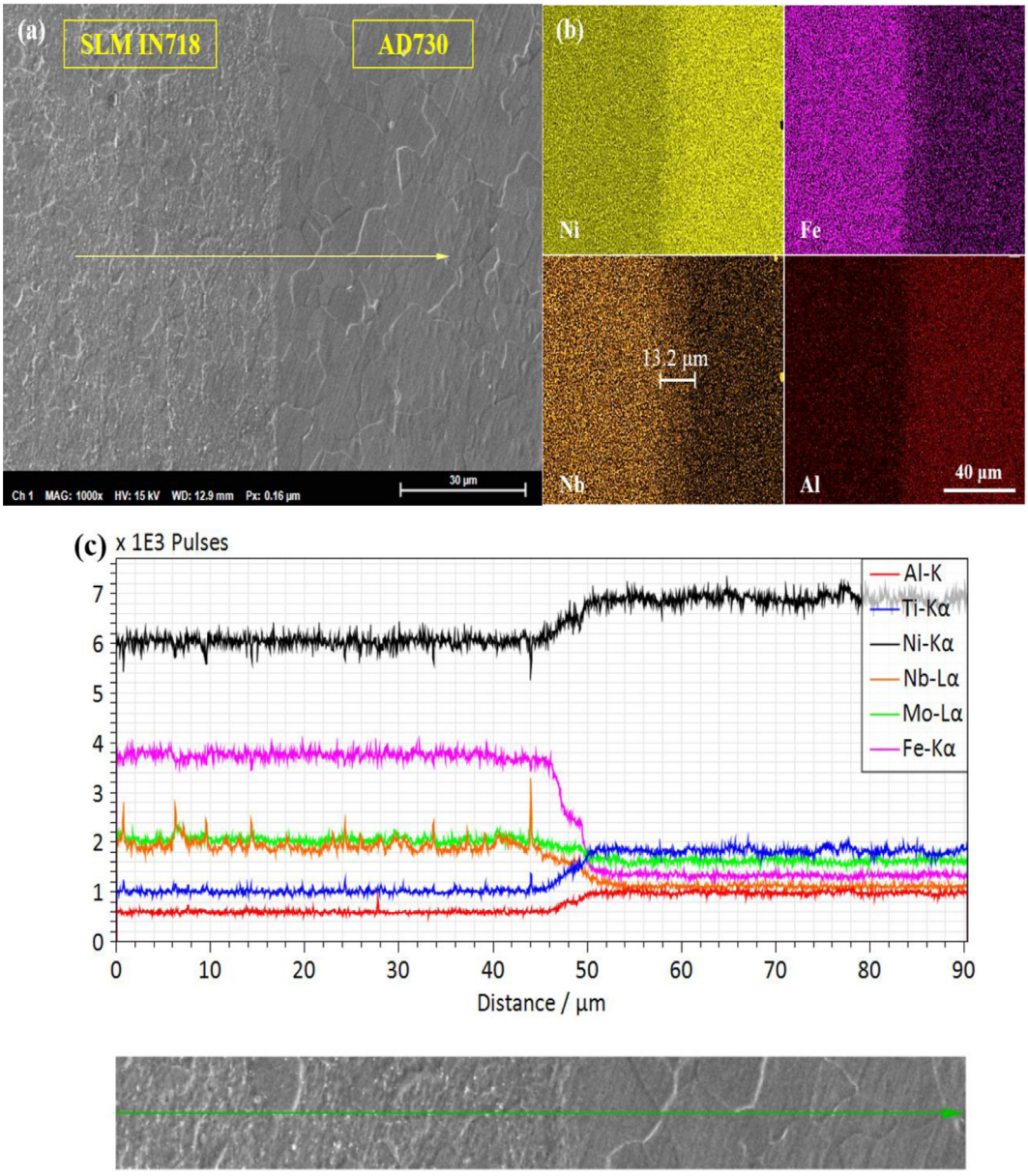

Fig. 3. (a, b) SEM image and EDS map of the analyzed regions in both superalloys across the weld line. (c) Line analysis with length 90 μm corresponding element profiles across the weld line.

At least five-line measurements were carried out at different distances.

3. Results and discussion

3.1. Chemical compositional change

The compositional changes in each matrix were micro-analyzed by EDS across the weld line. EDS map scanning of major elements (Ni, Fe, Al, Ti, Nb, and Mo) was carried out at 90 μm (Fig. 3). The diffusion profile of each element could be seen as a "plateau" for the as-welded bi-metallic welds. The distribution of elements such as Ni, Fe, Al, Ti, Nb, and Mo, in the intermixed region near the weld line is and evidence of their diffusion profiles revealed by the EDS line scan across the interface. Atoms were displaced from alloy with the higher content to alloy with the lower content. The diffusion per se depends on the inherent diffusion coefficient of each atom. As an example, Fig. 3(b), presents the diffusion of Nb from SLM IN718 alloy over a distance of about 13.2 μm. This diffusion distance for each element can be affected by thermomechanical parameters, which are considered in the following sections (3.2 and 3.3) of this study.

The combination of rapid heating and sever plastic deformation during LFW assisted the diffusion of these elements on both sides of the contact surfaces and the formation of the transition regions. That is why Fe, Mo, and Nb atoms migrated from SLM IN718 towards AD730^{TM} and Ni, Al, and Ti diffused from AD730^{TM} to IN718 resulting in the bonding at the weld interface. Senkov et al. [23] reported the same trends for IFW of dissimilar Mar-M247 and LSHR superalloys.

The mutual diffusion of elements between dissimilar alloys could provide a strong metallurgical bonding without forming any harmful intermetallic compounds such as γ/γ' eutectic and/or liquation under LFW high temperature compression. Such elemental diffusion could alter the local chemical composition of precipitates like Laves phase close to the weld line of SLM IN718, which is

commonly found in friction-welded Ni-based superalloys [21]. The diffusion of heavy elements such as Nb and Mo as constitutional elements of the Laves phase in IN718 decrease the volume fraction of this phase near the weld line in WZ due to their dissolution at high temperatures (1200–1250 °C) and drastic plastic staining in the weld region. As a consequence, the mechanical properties of both SLM IN718 and AD730^{TM} can be altered (through the increasing solid solution strengthening mechanism). AD730^{TM} alloy experienced less deformation and mechanical mixing than SLM-IN718, resulting in less extended transition region on the AD730^{TM} side. Similar results were also found in dissimilar inertia friction welding of Mar-M247 to LSHR [23], U720Li to IN718 [26], IN718 to SM45C steel [36], and IN718 to Ti6Al4V [37], where the transition regions were larger in alloys presenting a lower volume fraction of strengthening phase.

3.2. Precipitates distribution analysis

Apart from variations in grain size and misorientations in different zones of the LFW joint on both sides [35], significant changes were also observed in the volume fraction, morphology, and distribution of the second phases (e.g., γ' and Laves). Figs. 4 and 5(a) illustrate size and volume fraction variations of different γ' vs distance from the weld interface. A trimodal distribution of γ' particle fractions (γ_p' (9%), γ_s' (27%), and γ_t' (2%)) was revealed in the BM zone in forged AD730^{TM} alloy where the microstructure prior LFW was unaltered.

Masoumi et al. [34,38,39] investigated the precipitation of secondary phases (all types of γ') in LFW of AD730^{TM}. They reported that the gradient in deformation rates affected the kinetics of dissolution and re-precipitation of γ' phases. Furthermore, the different primary, secondary, and tertiary γ' sizes could also affect their solvus temperatures.

With a decrease in distance from the weld interface, the γ' precipitates volume fraction and size were decreased. As shown in Fig. 4(a) and (b), close to the WZ and in the TMAZ, primary γ' precipitates are located mostly on grain boundaries. The γ_p' particles started to be dissolved from 0.3 mm, while γ_s' and γ_t' were dissolved at a distance of 1 mm from the weld line. The total volume fraction of all forms of γ' precipitates at 1 mm from the weld interface was similar to that of the initial BM.

As shown in Figs. 4(d, e) and 5(a), both intergranular and intragranular γ' were distributed in the BM as a function of the distance between the weld line and beyond 1 mm from it. The particle size distribution for γ_p' typically varied between 0.7 and 3.2 μm from the WZ to the BM; respectively, 200 to 700 nm for γ_s', and 30 to 90 nm for γ_t' in the BM zone. Fig. 5(a) demonstrates that the LFW process has caused significant dissolution of all forms of γ' in the WZ. It is observed that toward the weld line, first, γ_t' was dissolved, followed by γ_s' and finally, fine γ_p'. This finding indicates that TMAZ width is around 1 mm (Figs. 4 and 5), where an increase of the fraction of γ_p' was revealed from the WZ. It must be emphasized that it is very difficult to fully suppress γ' precipitation while cooling from a partially/fully solutionized temperature to the room temperature. The dissolution behavior of different γ' reveals the existence of different thermal gradients exist from the weld line to the BM. Masoumi et al. [38,40] reported that, in AD730^{TM} alloy, the full dissolution temperatures of primary, secondary, and tertiary γ' are around 1220 °C, 1120 °C, and 850 °C, respectively. As a result, it is supposed that the welding temperature at the WZ, which can be affected because of a high heating rate (~ 350–400 °C s^{-1} [18,31]), which was achieved at least 1220 °C (1200–1250 °C).

Figs. 5(b) and 6 show the evolution of Laves particles and microstructure in SLM IN718 at different locations from the weld line to the BM region. The distribution of Laves particles in the IN718 was investigated in both pre-weld (in HAZ and BM zones [41]) and post-weld conditions. Fig. 6(a, b) shows spherical (or semi-spherical) Laves particles within the grains in the WZ. From the WZ to the BM, the shape of the Laves phase was changed from spherical to long-striped (irregular and elongated particles with bigger aspect ratio) in the interdendritic regions in the HAZ and BM. In the TMAZ (Fig. 6(c)), the volume fraction of this phase increased. In the HAZ (Fig. 6(d, e)), both spherical and long-striped shapes precipitates could be observed in the blocky zones which is in agreement with the investigation reported in [41].

As well AD730^{TM} side, in addition of grain size and misorientation changes in different zones of the LFW joint, a significant change was also observed and the volume fraction and distribution of the Laves particles (white particles) as well as the Nb content in them were quantified. As shown in Fig. 5(b), the volume fraction of the Laves phase and Nb content were increased from the WZ to the BM.

The laves phase volume fraction was increased as a function of the distance from the weld line. Furthermore, the amount of Nb as one of the constitutional elements of Laves phase $(Ni,Cr,Fe)_2(Nb,Ti)$ was increased. The Laves phase particles were dissolved within the matrix at the WZ. The lower amount of Nb in the Laves and also the lower fraction of this phase at the WZ reveal that during LFW, the temperature was high enough beyond 1150 °C and led to dissolve the Laves and redistribution of Nb by short-range diffusion to the matrix.

3.3. Effects of thermomechanical compressive strain

In the TMAZ, in addition to grain size, the volume fraction of the Laves phase was higher than the WZ due to their different thermal gradients, heating and cooling rates, and drastic reductions in compression effects (or strain). It has been reported [42,43] that the diffusion of solutes in the matrix increases exponentially with compressive strain as:

$$D_s = D.\exp\left(-\frac{Q'S}{KT}\right) \quad (1)$$

where D_s and D are respectively the diffusion coefficients under strain and free loading conditions. Q'= dQ/dS is the variation of activation energy of diffusion (Q) due to the change of the strain (S) (negative for compressive strain and positive for tensile strain). K and T as the Boltzmann's constant and the temperature (in Kelvin), respectively. Kringhøj [44] reported that the vacancy-assisted mechanisms are dominant for elemental diffusions at high temperatures in the matrix. Energy calculations [44,45] showed that the formation energy of the vacancies decreases with applied compressive strain. According to Eq. (1), at high temperatures, the application of compressive forging loads (strain at forging stage is equal to ~ −24.9) can enhance the diffusion processes of the solute elements into the matrix at high temperatures whereas imposing tensile strain slow down the processes.

It should be noted that recrystallization was not observed in the HAZ. However, in some zones the so-called blocky zones, with interdendritic Laves precipitates were partially dissolved leading the diffusion of Nb and Mo into the γ matrix of SLM IN718 (Fig. 6(d, e)). As reported by [41], the thickness of HAZ was controlled by the heating and cooling rates and the shape of the Laves phase was changed from long-striped to spherical within the blocky zones. Hence, due to enough equivalent time (t_e) and temperature (T) controlling the diffusion of elements from the core of the dendrite into interdendritic regions, no liquation and eutectic composition were found in the HAZ. The influence of the heating/cooling rates, time (15.4 s), and temperature (1200–1250 °C), on the diffusion distance (x) in the HAZ, was reported by Tabaie et al. [41]. In this

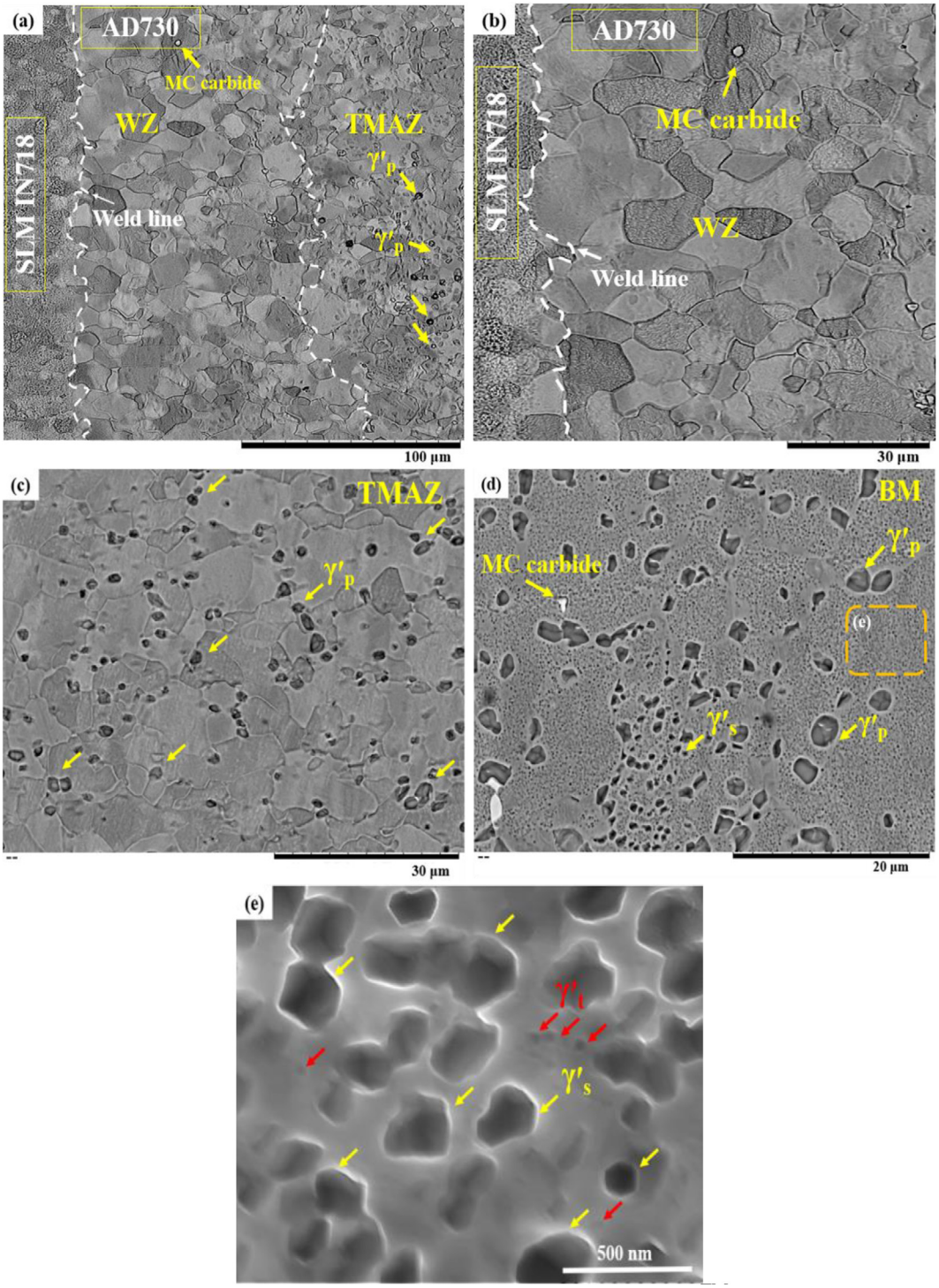

Fig. 4. FE-SEM images of different γ' precipitates in LFWed AD730™ and SLM-IN718 (a, b) at the WZ and weld interface, (c) in the TMAZ or ~0.2 to 1 mm from the weld interface, and (d) (e) secondary (γ'_s) and tertiary (γ'_t) γ' in the BM of AD730™.

model x can be estimated by considering the strain assisted diffusion changes in the TMAZ:

$$x = \sqrt{D_e t_e} \tag{2}$$

$$D_e = D(m^2/s) = 1.04 \times 10^{-6} \exp(-201700/RT) \tag{3}$$

where t_e is the equivalent holding time for the entire diffusion process acting at different stages (heating + holding + cooling cycle). R is the universal gas constant, Q (201,700 J mol^{-1}) is the equivalent activation energy for the diffusion process of Nb in Ni, T is the equivalent temperature during LFW. The activation energy and temperature values used in Eqs. (2-5) were obtained from reference [41]. For the HAZ, the diffusion coefficient of Nb in Ni can be estimated from D_e (Eq. (3)). As a result, in the TMAZ, where is affected by both the temperature (high heating rate) and compressive strain, the diffusion distance can then be estimated as (replacing Eqs.1 and 3 in Eq. (2)):

$$x = \sqrt{D_s t_e} \tag{4}$$

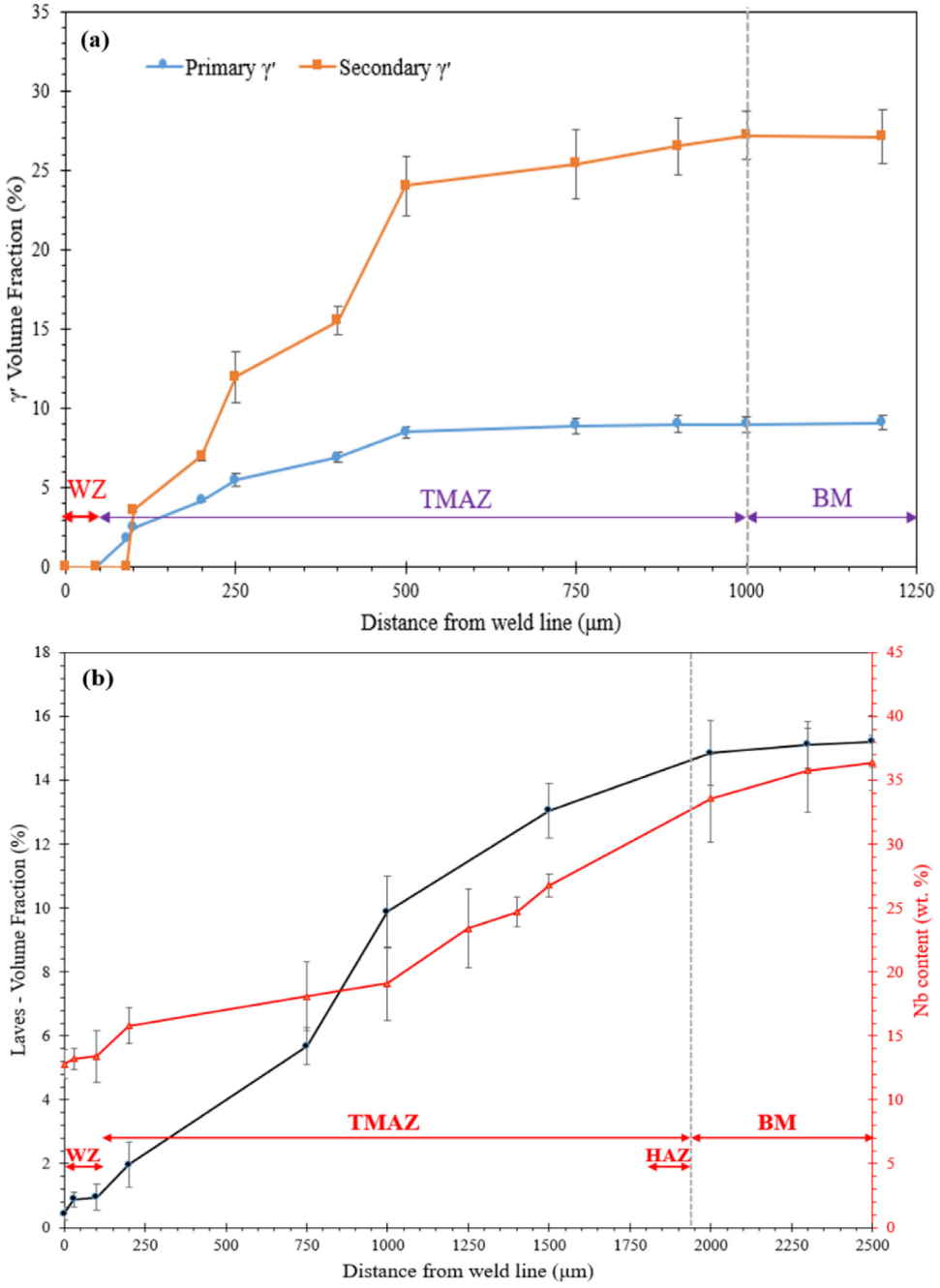

Fig. 5. Variation of (a) volume fraction of γ' in AD730^{TM}, and (b) Laves phase and Nb content in the Laves particles in SLM IN718 as a function of the distance from the weld interface.

$$\rightarrow \; x = \sqrt{D_e . \exp\left(-\frac{Q'S}{KT}\right) . t_e} \tag{5}$$

On the basis of Eq. (5), it was found that the diffusion distance (x) increased during the forging stage of the LFW process where important compressive strains are applied to the interface. In the above calculations, it was assumed that the weld line temperature was in the 1200–1250 °C range and the heating and cooling rates were 350–400 °C s^{-1} and 50–80 °C s^{-1}, respectively. Specifically, the maximum value of x, in the absence of any applied strain, was 385 nm, while this value was increased by almost 7–10 times after applying the compressive strain.

The Nb contents, in the bulk of the matrix, were measured for 5.1 wt.% and 1.1 wt.% in as-SLM IN718 and AD730^{TM}, respectively. However, by segregating Nb and Mo at interdendritic regions during the solidification, the Laves phase could form in SLM IN718. Hence, the Nb concentration in the matrix close to the Laves phase in dendrite (3.33 wt.%) was lowered. As shown in Fig. 7, the amount of Nb in the matrix of the SLM IN718 side increased from 4.48 ± 0.32 (wt.%) at a distance of 60 μm to 4.81 ± 0.18 (wt.%) at a distance of 20 μm from the weld line (in the WZ), while the Nb concentration decreased close to the weld line (4.3 ± 0.3 wt.% at 10 μm, point 1). In AD730^{TM} alloy, the Nb content close to the weld line was higher than the bulk and decreased as we move away from the weld line. Therefore, it indicates that the Nb concentration in the matrix increased from the BM to the WZ (in SLM IN718) due to the dissolution of the Laves phase and its diffusion back to the matrix. However, very close to the weld line, the compressive

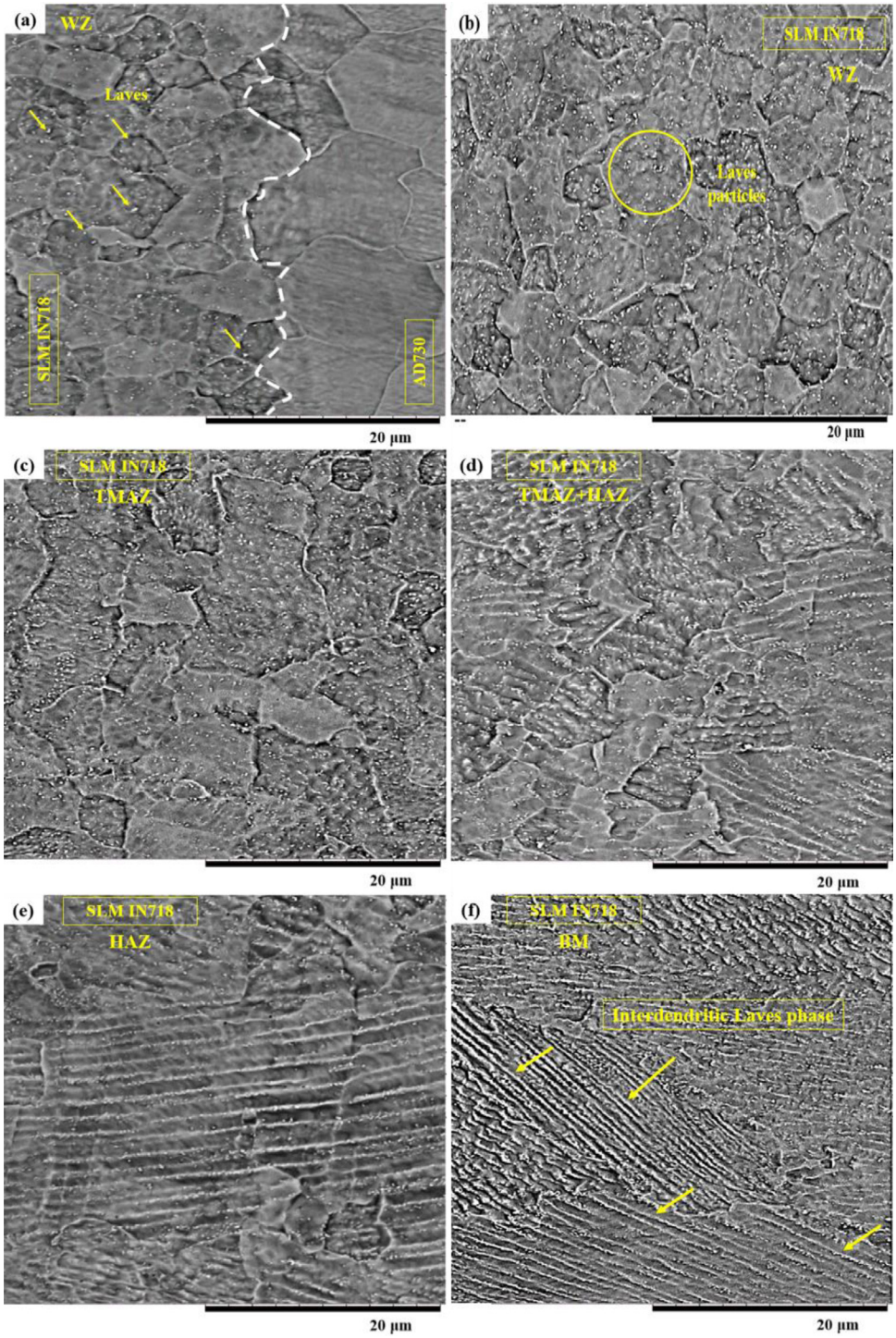

Fig. 6. SEM images of the microstructural evolution in SLM-IN718 after LFWed to AD730^{TM} alloy: (a, b) the weld line and spherical Laves particles formed in the WZ, (c, d) the TMAZ, (d, e) HAZ with mixed spherical and long-striped Laves particles, and (f) the BM with long-striped interdendritic Laves.

strain was more effective than the temperature on elemental diffusion, leading to a more extended diffusion distance (x) and migration into AD730^{TM}.

High compressive strain levels leading to a total axial length shortening of about 3.3 mm (2.14 mm for SLM IN718 and 1.16 mm for AD730^{TM}) increase the diffusivity (by 7–10 times) of constituent elements of secondary phases (e.g., Nb in Laves phase) into the γ matrix, as reported in Table 2 and Fig. 7(b). As the presence of γ' and Laves particles above their solvus temperatures (i.e., ~1200 °C and 1150 °C, respectively) is a prerequisite for their liquation, the "accelerated" dissolution of these particles can reduce or even suppress the propensity for γ' and Laves liquation.

In the present study, the liquation phenomenon was not observed on the AD730^{TM} side of the joint. On the SLM IN718 side, although liquation was expected, due to the applied high temperature (greater than the eutectic Laves/γ temperature), no liquation was observed in the WZ, the TMAZ, and the HAZ. This behavior can be attributed to the high heating and cooling rates and applied compressive strain during LFW.

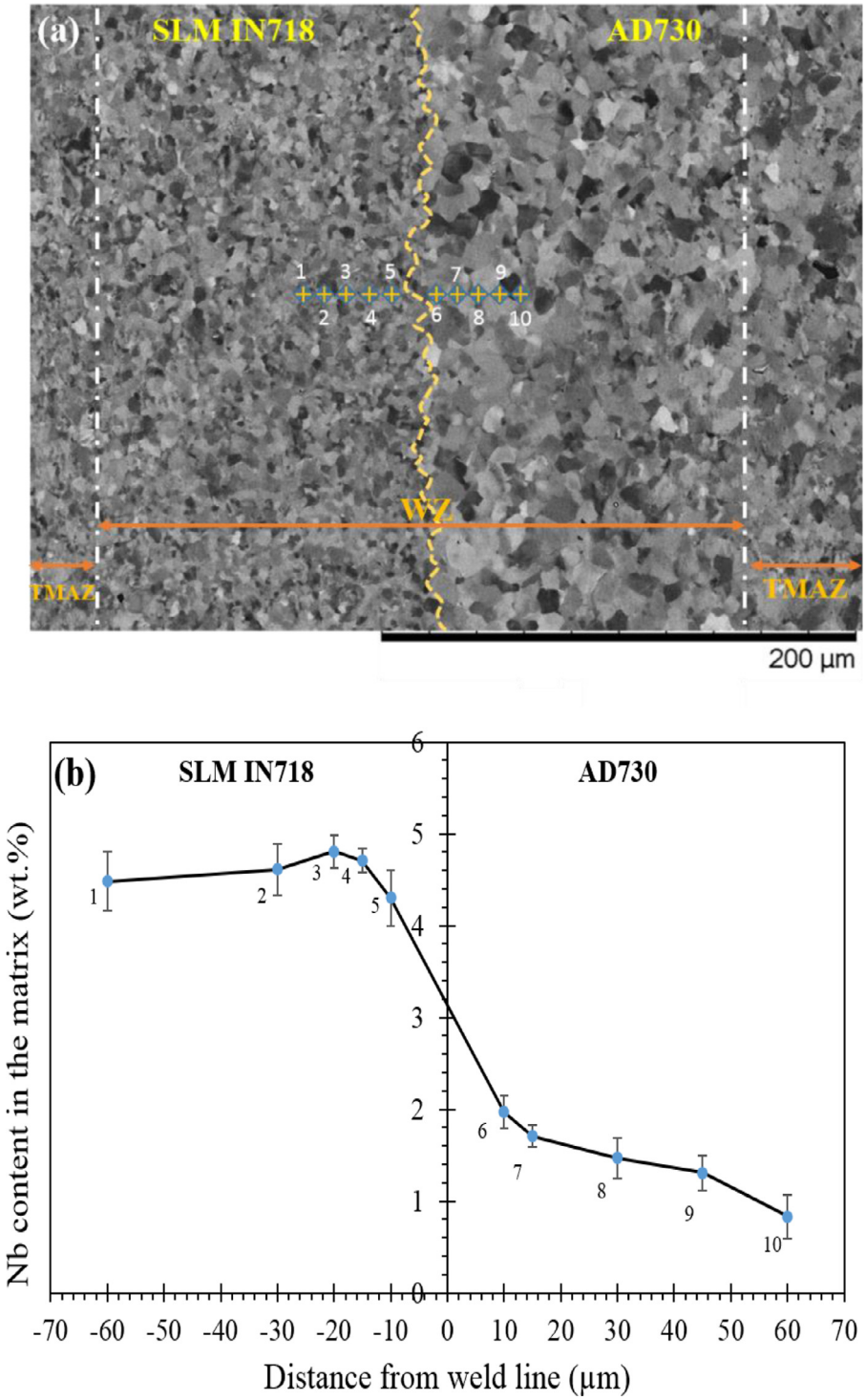

Fig. 7. (a) SEM micrograph from the weld line, (b) variation of Nb in the γ matrix obtained from different EDS spot analysis in both superalloys close to the weld line after LFW.

The local elastic field in the vicinity of the interfacial dislocations may promote the acceleration of the diffusion processes and of the $\gamma + \gamma' \rightarrow \gamma$ reaction. Giraud et al. [46] reported that the applied stress/strain at high temperature enhances the secondary phase (γ') dissolution kinetics.

At low temperatures, solute atoms have low mobility within the lattice, while at higher temperatures, they become mobile along with dislocations [47]. The accumulation of solute atoms in mobile dislocations further strengthens the obstacles (e.g., pile-up dislocations), raising the critical stress needed to overcome these obstacles. When the applied flow stress exceeds the critical stress, these mobile dislocations move to the next obstacles (with increased strain and relaxed stress). Therefore, increased high-temperature plastic deformation, in combination with the applied stress, promote precipitate dissolution and increase dislocation density (ρ_d) (see Eq. (6)). This, in addition to lattice diffusion, enhances the ef-

fective pipe diffusion coefficient (D_{peff}), particularly at the γ/γ' interfaces [46,48]:

$$\rho_d = \frac{10}{b^2}\left(\frac{\sigma}{\mu}\right)^2 \quad (6)$$

$$D_{Peff} = \rho.a_p.D_p \quad (7)$$

where ρ_d, b, and μ are the dislocation density, the Burger's vector, and the shear modulus of the alloy under applied stress, respectively. The parameter of $a_p.D_p$ is the pre-exponential term of pipe diffusion for Ni alloys (3.1×10^{-23} m^4 s^{-1}). a_p is the cross-sectional area of the dislocation pipe in which fast diffusion is taking place. The values of applied frictional and forge pressures (σ) during linear friction welding were 220 and 340 MPa (total process time t_p = 15.4 s), respectively. As reported by [34], lattice and pipe diffusion can enhance the self-diffusivity of the elements and influence the extent of liquation in the LFW process. According to Eqs. (6) and (7), the application of compressive stress during LFW (at maximum temperature of 1250 °C) results in by 33 and 31 times increase in the diffusivity in the matrix of SLM IN718 and AD730^{TM}, respectively. On LFW of AD730^{TM} [34], Masoumi et al. reported that with an applied forge pressure of 265 MPa (t_p = 10 s), the diffusivity increased by around 25 times, and no liquation was observed. While for LFWed IN738 [49] with an applied forge pressure 90 MPa (t_p = 21.6 s), the diffusivity increased by 3.35 times and intergranular liquation, caused by non-equilibrium phase reactions, occurred in the microstructure. However, the occurrence of liquation was suppressed in LFW of Waspaloy [45] by applying specific LFW conditions which increased the diffusivity by 3.7 times (applied friction pressure 90 MPa, t_p = 4.4 s, and temperature in the weld line measured at 1220 °C). As a result, the increase in the dissolution kinetics of secondary phase with the level of plastic deformation (friction and forge pressures) may be due to an enhanced diffusion by dislocation pipe diffusion mechanism. In addition to an applied higher stress (e.g., in this study and similar welding of AD730^{TM}), a shorter process time at high temperatures during the LFW process (e.g., similar to LFW of Waspaloy) can reduce the liquation in the microstructure.

Although less strain (35% of total axial shortening) was applied to AD730^{TM} alloy as compared to SLM IN718, the effect of compressive strain was more significant on the dissolution of its secondary phases than of the Laves phase in SLM IN718, due to the complete dissolution of the γ' phases in the WZ on the AD730^{TM} side. It should be noted that the complete dissolution of the Laves phase needs higher temperature and more time for inter-diffusion of Nb and Mo, as compared to the diffusion of Al and Ti to the matrix, as also reported by [50,51]. Therefore, the impact of this phenomenon on the mechanical properties of the joint needs to be investigated, and this is done in Section 3.4.

In addition, the absence of liquation (and liquation cracking) and eutectic compositions (γ/γ' and γ/Laves) could be explained by the parameters that influence particle liquation and subsequent cracking during friction welding. As reported by Smith et al. [30], rapid heating-up in LFW (300–500 °C s^{-1}) altered the thermodynamic equilibrium conditions that can favor the early re-melting of grain boundaries, and later, their rapid solidification (non-equilibrium) through an increase of elemental diffusion (intergranular liquid film migration). Moreover, Ola et al. [49,52], who simulated the LFW of superalloy Inconel 738 (IN738) and a single crystal superalloy by Gleeble, reported the effect of stress-induced compressive strain (in the WZ and the TMAZ) on back-diffusion, which controls the isothermal re-solidification of intragranular metastable liquid. They observed that imposing compressive strain significantly aided the re-solidification of the intragranular liquid, where increased the diffusivity of solute atoms resulted in enhanced back-diffusion and healing. Therefore, under compressive strain (at the forging stage of LFW), the diffusion of a solute atom can be enhanced in the WZ and the TMAZ.

Despite the absence of a compression strain in the HAZ, no liquation was observed in that region due to the influence of the high heating rate (100–200 °C s^{-1}) on increasing the elemental diffusion (Nb and Mo) at the interdendritic region [41]. Moreover, Ojo et al. [53] and Vishwakarma et al. [31] reported another mechanism for suppressing liquation by the diffusional coherency strain in the HAZ due to the atomic size mismatch between secondary phase constituent elements and matrix atoms in IN738 alloy. This mechanism can cause intergranular liquid film migration (LFM), where no externally applied stress is involved. On the contrary, by applying externally compressive stress/strain during LFW, the initiation of LFM is controlled by lattice solute back-diffusion and can be aided by strain-enhanced diffusivity. As a result, eliminating both intergranular and intragranular liquid films in the HAZ during LFW was achieved by a combination of rapid heating and cooling, solute back-diffusion, and LFM.

3.4. Microhardness

The effects of grains size and misorientation on the microhardness of this joint are reported in Ref. [35]. The microhardness variations across the weld line toward the BM zone on both sides are shown in Fig. 8. The average microhardness of the BMs in AD730^{TM} and SLM IN718 superalloys is respectively 393 and 340 HV (which are similar to the hardness of the alloys before LFW). The hardness in SLM IN718 decreased from 281 ± 9 HV at −500 μm from the weld line to 236 ± 4 HV close to it. The lowest hardness (236 HV) was measured at ~115 μm from the weld line. The average measured hardness on the AD730^{TM} side increased from 364 ± 11 HV at +1000 μm from the weld line to 443 ± 7 HV close to it. The highest hardness (443 HV) was found at 85 μm from the weld line.

The hardness in AD730^{TM} decreased from the WZ toward the TMAZ (until ~ 1000 μm), and then increased towards the BM up to 393 ± 4.5 HV. In SLM IN718, after the TMAZ, the hardness continuously increased from the WZ (236 ± 4 HV) to the TMAZ (281 ± 9 HV), and then increased up to 341 ± 8 HV in the BM. As shown in Fig. 8, close to the BM in SLM IN718, the hardness increased in the HAZ, having a thin layer (20–60 μm), and then decreased again toward the BM.

The microstructure in the WZ could be homogenized due to the high temperature generated during LFW (1200–1250 °C). AD730^{TM} presents the hardening behavior, while SLM IN718 presents softening, as also reported by other authors when IN718 is welded to other alloys with higher strengths [17,54,55]. As mentioned, the strengthening phases were completely dissolved in the WZ. This means that no precipitation hardening was expected in this region. Therefore, the observed hardness variation in the WZ can be attributed to grain size changes according to the Hall-Petch relationship [21]:

$$\sigma_y = \sigma_0 + k_y.d^{-1/2} \quad (8)$$

where σ_y is the yield stress, σ_0 is the friction resistance for dislocation movements in the slip bands, k_y is the Hall-Petch parameter and d is the average grain size. It is known that the yield stress can be empirically related to the microhardness. As the WZ is free of secondary phases, microhardness variations can basically be related to the grain size. However, the evolution of the microhardness in the WZ is different in SLM IN718 as compared to AD730^{TM} superalloys.

In the WZ of SLM IN718 at 250 μm from the weld line, the grains size increased from 2.25 to 5 μm, but the decrease of the hardness did not obey the Hall-Petch relationship, whereas in

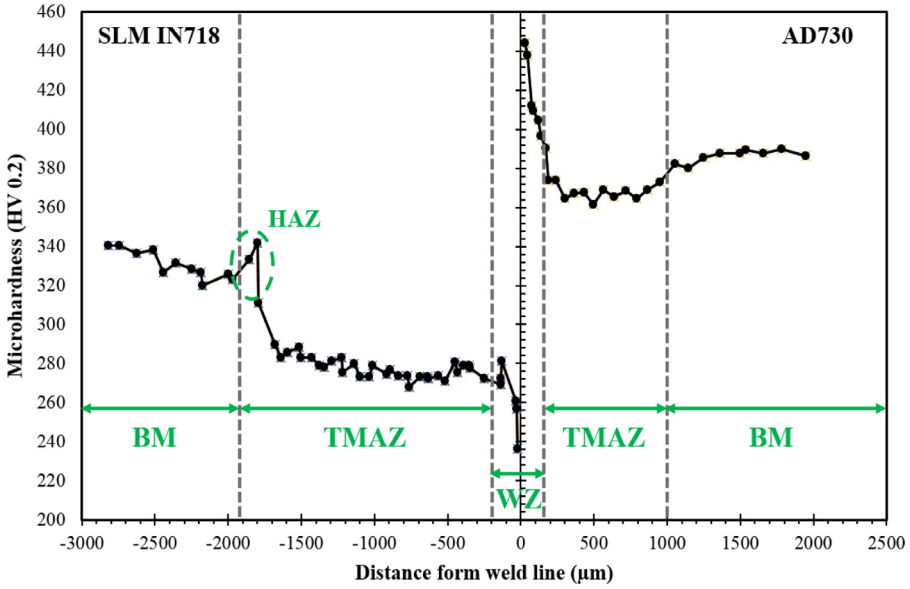

Fig. 8. Microhardness profiles as a function of distance from the weld line of two LFWed samples.

AD730^{TM}, the microhardness increased with the grains size decrease according to this relationship. Although all precipitates (except MC carbides) were dissolved in the WZ on both sides of the weld line, the different hardness behavior variations reveal that the contribution of second phase to the strength of IN718 alloy is higher than the one from grains size refinement as also reported by [50]. The same trends are also found in dissimilar joint after LFW of IN718 to IN713LC [21]. The effect of other hardening mechanisms (e.g., matrix solid solution strengthening, grains misorientation, and pile-up dislocations at grain boundary) has been discussed in a recent publication by the present authors [35].

In the TMAZ, the hardness in the SLM IN718 is lower than the BM (−21%) and higher than the WZ (+16%). It is expected that elements such as Ni, Mo, Al, and Ti forming the secondary phases (Laves, γ'/γ" and δ) diffused to the matrix, will slightly increase the hardness by solid solution strengthening [13,56]. In the TMAZ, the effect of compressive strain is less than WZ. However, the diffusion distance (x) of Nb at 1000–1150 °C, even without considering the strain Eqs. (2) and ((3)), could reach 294–306 nm (knowing that the dendrite arm spacing is 820 ± 130 nm). Therefore, the secondary phases, the solid solution, plastic strain, and grain size can affect the hardness of the TMAZ. The hardness of AD730^{TM} showed a decrease in the TMAZ due to the dissolution of γ' particles, and an increase in hardness by the grain refinement in the WZ. It must be emphasized that although the grain size increased after the TMAZ toward the BM (from 5 to 52 μm for SLM IN718 and 10 to 41.36 ± 9.14 μm for AD730^{TM}), the hardness is greater in the BM than in the TMAZ. This indicates that in these regions the hardness is less affected by the temperature and deformation (strain and strain rate), and here, secondary phases (γ', Laves, and γ'/γ") remained undissolved during the LFW process.

In SLM IN718, in the narrow HAZ, between the TMAZ and the BM, the hardness increased as compared to the BM presumably due to the partial dissolution of Laves phases (mixture of spherical and long-striped shapes), the diffusion of Nb and Mo in the matrix (solid solution), and the remaining strengthening phases (e.g., γ" in size of ~80 µm) in the blocky zones, as also reported by [41]. Therefore, the effect of the Laves phase on the yield strength is achieved by influencing the volume fraction, the size, and the distribution of γ" phase due to the effect of high heating rate [4,41,57].

In the BM zone, secondary precipitates such as Laves phase plus γ' and γ" phases could remain in the microstructure, as also reported by [58]. On the SLM IN718 side, as the distance is increased from the weld line, the hardness increases continuously until reaching that of the BM. Furthermore, despite the larger grain size in the BM, its hardness is more than the WZ and the TMAZ, which can be attributed to the formation of cellular substructures and dendritic/cellular segregation occurred due to the high cooling rates during the SLM process. The grain boundaries and the sub-grain boundaries are highly decorated with micro-segregated particles (Laves phases and to some extent MC carbides) (Fig. 6(f), white particles) [50]. These sub-grain boundaries contained precipitated particles and high density of dislocation networks [50,59]. The boundaries between cellular microstructure induce more dislocation interactions and hamper dislocation movements which can increase the hardness of the alloy by dislocation strengthening mechanism. However, the hardness in the BM was lower (~7%) than in the HAZ, due to the long-striped shape of Laves particles in the BM, which can reduce the strength and ductility of the alloy, as also reported by [41] and Sui et al. [57].

As a result, in the SLM IN718, the contribution of precipitation hardening mechanism (plus contribution of dislocation strengthening) is more than grain refining effects. On the contrary, on the AD730^{TM} side, although the grains size in the BM is larger than in the TMAZ, its hardness was higher (by ~10%) due to the presence of primary, secondary, and tertiary γ' phases. This points to a significant effect of precipitation on the strength (σ_{ppt}) and its impact on dislocation movement or strengthening by dislocation (σ_{dis}). However, the effects of solid solution (σ_{ss}) and grain size or grain boundary movement (σ_{gb}) mechanisms are generally higher than others in AD730^{TM} alloy. The possible contribution of ultrafine γ' precipitate (γ_{p}', 2–10 nm) to the strength of the alloy should also be considered in the WZ. As reported by several authors [38,60] the complete dissolution of γ_{p}' in AD730^{TM} in the temperature range experienced during the LFW process is unlikely. On the other hand, it is also possible that some ultrafine γ' precipitate form during the post weld cooling step. However, in the present work such precipitates were not observed in the microstructure indicating that the selected LFW conditions resulted in the absence of precipitates in the final microstructure of the WZ. Therefore, in the analysis of the results, no contribution to the hardness of the alloy

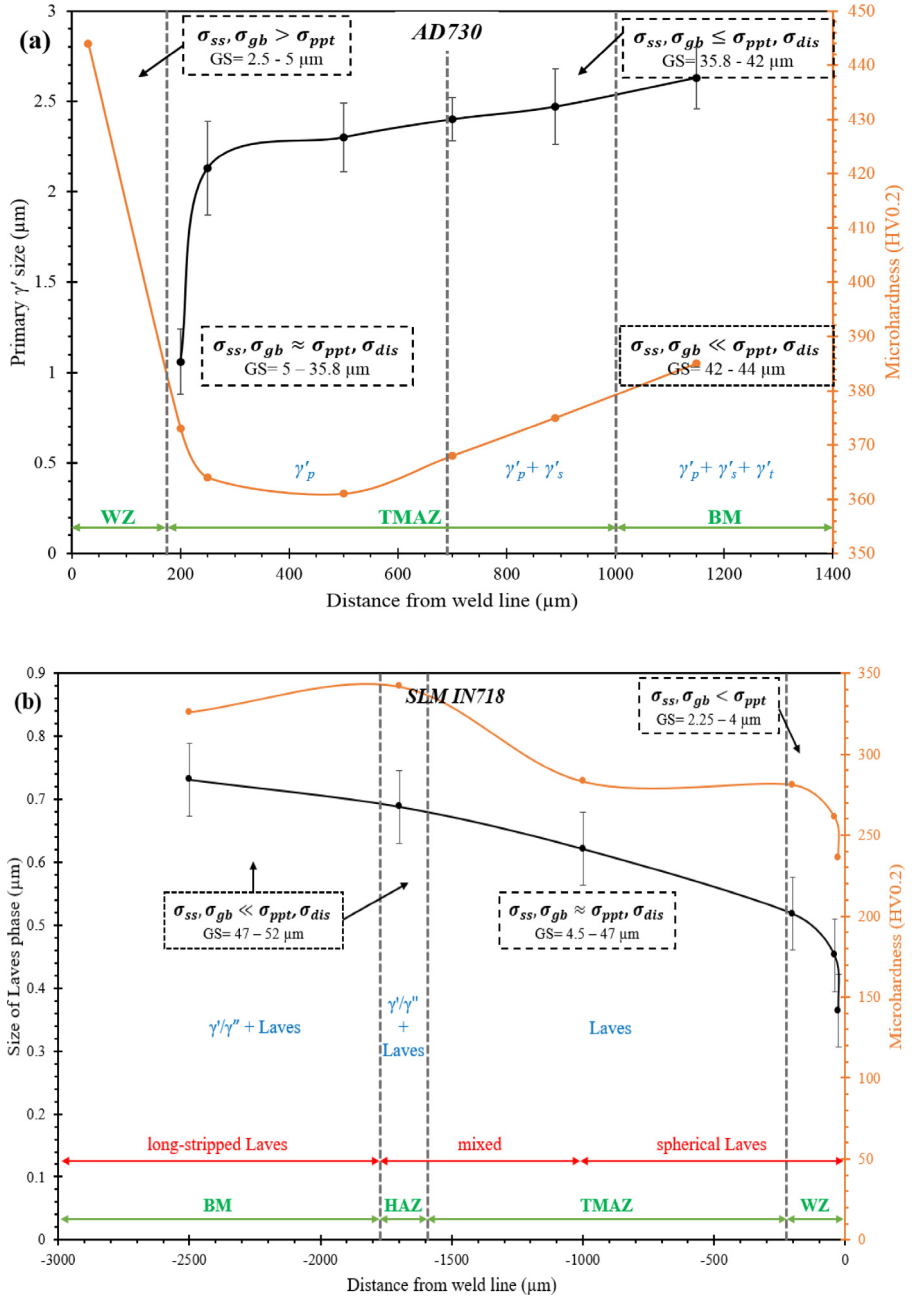

Fig. 9. Variation of hardness and the size of secondary phases with distance from the weld line on (a) AD730^{TM} and (b) SLM IN718 sides.

is considered. It must be noted that, even if some precipitates are present, undissolved during heating or formed during cooling, the contribution to the strength should be negligible. Finally, it is well known [21,61–63] that the hardness and other mechanical properties of similar and dissimilar alloys LFWed can be enhanced by applying proper post-weld heat treatment cycles through precipitation hardening.

3.4.1. Effects of secondary phases

According to Eqs. (9–14), the changes in the volume fraction (in accordance with the portion of elements in the composition of the Laves and γ'/γ'' phases and without δ phase) and the size of secondary phases (Fig. 9(a, b)) can alter the hardness.

In as-SLM IN718 [57]:

$$x_{\mathrm{Al-matrix}}(1 - f_{\mathrm{Laves}} - f_{\gamma'} - f_{\gamma''}) + x_{\mathrm{Al-Laves}} f_{\mathrm{Laves}} + x_{\mathrm{Al-}\gamma'\mathrm{Ni3Al}} f_{\gamma'-\mathrm{Ni3Al}} = x_{\mathrm{Al-total}} \quad (9)$$

$$x_{\mathrm{Ti-matrix}}(1 - f_{\mathrm{Laves}} - f_{\gamma'} - f_{\gamma''}) + x_{\mathrm{Ti-Laves}} f_{\mathrm{Laves}} + x_{\mathrm{Ti-}\gamma'\mathrm{Ni3Ti}} f_{\gamma'-\mathrm{Ni3Ti}} = x_{\mathrm{Ti-total}} \quad (10)$$

$$x_{\mathrm{Nb-matrix}}(1 - f_{\mathrm{Laves}} - f_{\gamma'} - f_{\gamma''}) + x_{\mathrm{Nb-Laves}} f_{\mathrm{Laves}} + x_{\mathrm{Nb-}\gamma''} f_{\gamma''} = x_{\mathrm{Nb-total}} \quad (11)$$

$$f_{\gamma'} = f_{\gamma'-\mathrm{Ni3Al}} + f_{\gamma'-\mathrm{Ni3Ti}} \quad (12)$$

In AD730^{TM} for different types of γ' phase:

$$x_{\mathrm{Al-matrix}}(1 - f_{\gamma'}) + x_{\mathrm{Al-}\gamma'\mathrm{Ni3Al}} f_{\gamma'-\mathrm{Ni3Al}} = x_{\mathrm{Al-total}} \quad (13)$$

$$x_{\mathrm{Ti-matrix}}(1 - f_{\gamma'}) + x_{\mathrm{Ti-}\gamma'\mathrm{Ni3Ti}} f_{\gamma'-\mathrm{Ni3Ti}} = x_{\mathrm{Ti-total}} \quad (14)$$

where $x_{Al-matrix}$, $x_{Al-Laves}$ and $x_{Al-\gamma' Ni_3Al}$ are the concentration of Aluminum (Al) element in the matrix, Laves phase and γ'-Ni_3Al phase, respectively; $x_{Ti-matrix}$, $x_{Ti-Laves}$ and $x_{Ti-\gamma' \ Ni_3Ti}$ are the concentration of Titanium (Ti) in the matrix, Laves phase and γ'-Ni_3Ti phase, respectively; $x_{Nb-matrix}$, $x_{Nb-Laves}$ and $x_{Nb-\gamma''}$ are the concentration of Nb element in the matrix, Laves phase and γ" phase, respectively; $x_{Al-total}$, $x_{Ti-total}$ and $x_{Nb-total}$ is the concentration of Al, Ti, and Nb in the material, respectively; f_{Laves}, $f_{\gamma''}$, $f_{\gamma'-Ni_3Al}$ and $f_{\gamma'-Ni_3Ti}$ is the volume fraction of Laves phase, γ" phase, γ'-Ni_3Al phase and γ'-Ni_3Ti phase, respectively.

As mentioned in Section 3.3, the accumulation of solute atoms in mobile dislocations around precipitates could further strengthen the obstacles and raise the critical stress needed to overcome these obstacles [10,64]. The obstacles could temporarily or permanently block dislocation movements. During the LFW process, solute atoms can free themselves from forest/pile-up dislocations to help dislocation movements via pipe diffusion. Several factors, such as anti-phase boundary energy (γ_{APB}) (207 and 378 mJ m^{-2} for γ' and γ'', respectively, in IN718 [47,65] and 264.8 mJ m^{-2} [66] for and AD730^{TM}, respectively) as a function of ordered γ' and coherent γ", volume fraction (V_f) and size (r) of γ'/γ", may affect the precipitation strengthening mechanism [14,21,38,39,65,67,68], which is generally characterized by a critical resolved shear stress ($\Delta\tau_{total}$). The strength of the material can be adequately accounted for mainly by the coherency hardening mechanism (Orowan looping being the other mechanism). According to Eqs. (15 and 16), the critical resolved shear stress increases with increasing γ_{APB} and particle size for underaged particles (ordered secondary and/or tertiary γ' in AD730^{TM} and ordered-coherent γ'/γ" in SLM IN718), whereas for overaged or large particles (ordered primary γ_p' in AD730^{TM}), the critical resolved shear stress increases with increasing V_f, γ_{APB}, and decreases with increasing particle size (Eq. (17)). Furthermore, based on the coherent strain strengthening mechanism [47,69], the interaction of the dislocations and the stress field generated around the γ'' precipitates in IN718 plays a crucial role in the strengthening (more effective than γ' [11]) (Eq. (18)) [11,65,67,70]. The effect of the size of strengthening phases on the hardness results for both alloys is shown in Fig. 9.

$$\Delta\tau_c = \frac{\gamma_{APB}}{2b}\left[\left(\frac{6\gamma_{APB}V_f r}{\pi T}\right)^{\frac{1}{2}} - V_f\right] \text{(in both alloys)} \quad (15)$$

$$\Delta\tau_c = \frac{\gamma''_{APB}}{2b}\left[\left(\frac{\gamma''_{APB}V_{f\gamma''}}{\pi T}\right)\left(\frac{\sqrt{6}Rh}{3}\right)^{1/2} - \beta V_{f\gamma''}\right] \text{(in IN718)} \quad (16)$$

$$\Delta\tau_c = \sqrt{\frac{3}{2}}\left(\frac{Gb}{r}\right)V_f^{1/2}\frac{w}{\pi^{3/2}}\left(\frac{2\pi\gamma_{APB}r}{wGb^2} - 1\right)^{1/2} \text{(in AD730)} \quad (17)$$

$$\Delta\tau_{coherency} = 1.7G(\varepsilon)^{3/2}\left(\frac{V_{f\gamma''}(1-\beta)}{2b}\right)^{1/2}\frac{h}{R^{1/2}} \text{(in IN718)} \quad (18)$$

where b is the Burger's vector for the ⟨110⟩ dislocations (2.492 $\dot{A}$ for IN718 alloy [47,65] and 2.45 $\dot{A}$ for AD730^{TM} [71]), r is the size of the γ'/γ" particle, T is the dislocation line tension which is equal to $0.5Gb^2$, G is the shear modulus (average 75.4 GPa for γ'/γ'' in IN718 alloy [47,65] and 76.3 GPa for AD730^{TM} [71]), and w is a dimensionless constant (~1). ε is (= 0.498%–0.632%) the lattice misfit between the γ'' precipitate and the matrix. β, R, and h represent the constant ($\frac{1}{3}$) related to the distribution of γ" precipitates, the semi-major, and semi-minor axis lengths of the γ" precipitates, respectively [65]. The increased yield strength value is $\Delta\tau_{total}$ (sum of Eqs. (15-18) for each alloy). Therefore, the higher strength (hardness) of the material can be achieved by the coherent strain strengthening of the matrix, the precipitation of nanoscale γ'/γ" and microscale γ_p' phases (optimum size and number of particles [72]), and the dislocation interactions with particles.

A large volume fraction and fine particle size are generally beneficial for strengthening. The total strength can therefore be obtained as [10,12,14,64]:

$$\sigma_y = \sigma_0 + \sigma_{ss} + \sigma_{gb} + \sigma_{ppt} + \sigma_{dis}\,(\text{MPa}) \quad (19)$$

where σ_{ss}, σ_{gb}, σ_{dis}, and σ_{ppt} are contributions from solid solution strengthening, grain boundary strengthening, dislocation strengthening and precipitation strengthening, respectively. According to the Figs. 5, 8, and 9, the effects of the precipitation (size and volume fraction) mechanisms can be realized.

As mentioned above, and shown in Fig. 9(a), in the WZ of AD730^{TM}, the impact of grain size (and/or possible ultrafine undissolved precipitates) on the hardness of the material was more than precipitation. However, the effect of precipitation was more than grain size toward the BM due to increasing the size and volume fraction) of γ_p' (close to the grain boundaries) and γ_s' and the presence of γ_t' in the matrix (Fig. 5(a)). In Fig. 9(b), in the WZ of SLM IN 718, the grain size reduction could not increase the hardness and the strength of the material (according to the Hall-Petch relation). It reveals the significant impact of precipitation and the secondary phase dissolution (Laves and γ'/γ") on the strengthening of this alloy. From the WZ to the BM of SLM IN718, the hardness and probably strength of the alloy increased due to both undissolved secondary phases and small grains size (in the TMAZ). However, as revealed in the HAZ (Figs. 5(b) and 6(d, e)), the observed increase in hardness can be attributed to the sum of the contributions from the Laves phase, Nb micro-segregation, and γ" phase.

4. Conclusions

In this study, two Ni-based superalloys fabricated by two different methods, SLM IN718 and a forged AD730^{TM}, were linear friction welded. Variations of secondary phases across the weld line have been studied following welding. The impact of the evolution of the microstructure on the microhardness has also been evaluated. Various evolutions of microstructural features of SLM IN718 and AD730^{TM}, specifically the dissolving of secondary phases, alter the mechanical properties of LFWed parts. The main findings of this study can be summarized as follows:

(1) The different zones of LFWed joints were determined. The evolution of the precipitation or dissolution of secondary phases and microhardness as a function of strengthening mechanisms was found to be related to fundamental metallurgical features such as grain size variations and secondary phases.
(2) The microhardness evaluation of LFWed samples showed a drop in the hardness of the TMAZ in AD730^{TM} due to the dissolution of 90% of secondary γ' and all tertiary γ' volume fractions. On the other hand, with a decrease in distance from the weld line, the microhardness gradually increased due to grain refining in the microstructure.
(3) The strength of the SLM IN718 is more dependent on the secondary phases and their morphology as precipitation hardening mechanism than the grain size, whereas on the AD730^{TM} side, the effect of grain size (and/or even possible presence of ultrafine γ') on the strength of the alloy is more significant than that of secondary phases. This could be attributed to the absence of solid solution elements (e.g., Nb, Mo, W, Co, and Cr) in the chemical composition of secondary phases. However, both the size and the volume fraction of all phases affect the hardness and mechanical properties of the joint.

(4) A critical stress/strain is required to initiate plastic deformation at an appropriate process time range (10–15 s) to generate enough temperature (~1200 °C or higher than solvus temperature of secondary phases) to overcome the strength of the material during LFW.

Acknowledgments

The authors gratefully acknowledge the support from the Natural Sciences and Engineering Research Council of Canada (NSERC) 2018–03889 through a Discovery Grant. Thanks to Mr. Adrien Lieurey (IMT-Mines Albi ICA - site Albi) for his involvement and fabrication of SLM parts. They would also like to express their gratitude to Aubert & Duval Co., Dr. Alexandre Devaux, and Prof. Cormier for providing forged AD730™ samples and discussions on the definition of the scope of the project. Special thanks to TWI Ltd. for carrying out the LFW of the samples.

References

[1] A. Chamanfar, M. Jahazi, J. Cormier, Metall. Mater. Trans. A 46 (2015) 1639–1669.
[2] M. Cheepu, V. Muthupandi, W.S. Che, Appl. Mech Mater. 877 (2018) 157–162.
[3] A.R. McAndrew, P.A. Colegrove, C. Bühr, B.C.D. Flipo, A. Vairis, Prog. Mater Sci. 92 (2018) 225–257.
[4] Y. Cao, P. Bai, F. Liu, X. Hou, Metals (Basel) 9 (2019) 1128.
[5] A. Mostafa, I. Picazo Rubio, V. Brailovski, M. Jahazi, M. Medraj, Metals (Basel) 7 (2017) 196.
[6] E. Hosseini, V.A. Popovich, Addit. Manuf. 30 (2019) 100877.
[7] O. Adegoke, J. Andersson, H. Brodin, R. Pederson, Metals (Basel) 10 (2020) 996.
[8] T. Raza, K. Hurtig, G. Asala, J. Andersson, L.E. Svensson, O.A. Ojo, Metals (Basel) 9 (2019) 881.
[9] J.P. Oliveira, T.G. Santos, R.M. Miranda, Prog. Mater Sci. 107 (2020) 100590.
[10] R.W. Kozar, A. Suzuki, W.W. Milligan, J.J. Schirra, M.F. Savage, T.M. Pollock, Metall. Mater. Trans. A 40 (2009) 1588–1603.
[11] M.C. Chaturvedi, Y.-.F. Han, Met. Sci. 17 (1983) 145–149.
[12] N. Kamikawa, K. Sato, G. Miyamoto, M. Murayama, N. Sekido, K. Tsuzaki, T. Furuhara, Acta Mater 83 (2015) 383–396.
[13] O. Franke, K. Durst, M. Göken, J. Mater. Res. 24 (2011) 1127–1134.
[14] T.J. Ma, L.F. Tang, W.Y. Li, Y. Zhang, Y. Xiao, A. Vairis, J. Manuf. Processes 34 (2018) 442–450.
[15] X. Xie, J. Dong, G. Wang, W. You, J. Du, C. Zhao, Z. Wang, T. Carneiro, Superalloys 718 (2005) 287–298.
[16] A. Harte, M. Atkinson, A. Smith, C. Drouven, S. Zaefferer, J. Quinta da Fonseca, M. Preuss, Acta Mater 194 (2020) 257–275.
[17] C. Mary, M. Jahazi, Adv. Eng. Mater. 10 (2008) 573–578.
[18] F. Masoumi, D. Shahriari, H. Monajati, J. Cormier, B.C.D. Flipo, A. Devaux, M. Jahazi, Mater. Des. 183 (2019) 108–117.
[19] A. Chamanfar, M. Jahazi, J. Gholipour, P. Wanjara, S. Yue, Mater. Sci. Eng. A 555 (2012) 117–130.
[20] P. Geng, G. Qin, T. Li, J. Zhou, Z. Zou, F. Yang, J. Manuf. Processes 45 (2019) 100–114.
[21] R.R. Ye, H.Y. Li, R.G. Ding, T.J.A. Doel, S. Bray, A. Walpole, P. Bowen, Mater. Sci. Eng. A 774 (2020) 138894.
[22] O.N. Senkov, D.W. Mahaffey, S.L. Semiatin, Metall. Mater. Trans. A 49 (2018) 5428–5444.
[23] O.N. Senkov, D.W. Mahaffey, S.L. Semiatin, C. Woodward, Metall. Mater. Trans. A 45 (2014) 5545–5561.
[24] S.V. Lalam, G.M. Reddy, T. Mohandas, M. Kamaraj, B.S. Murty, Mater. Sci. Technol. 25 (2013) 851–861.
[25] H.Y. Li, Z.W. Huang, S. Bray, G. Baxter, P. Bowen, Mater. Sci. Technol. 23 (2007) 1408–1418.
[26] Z.W. Huang, H.Y. Li, M. Preuss, M. Karadge, P. Bowen, S. Bray, G. Baxter, Metall. Mater. Trans. A 38 (2007) 1608–1620.
[27] M. Karadge, M. Preuss, P.J. Withers, S. Bray, Mater. Sci. Eng. A 491 (2008) 446–453.
[28] A. Chamanfar, M. Jahazi, J. Gholipour, P. Wanjara, S. Yue, Metall. Mater. Trans. A 44 (2013) 4230–4238.
[29] T. Jokisch, A. Marko, S. Gook, O. Ustundag, A. Gumenyuk, M. Rethmeier, Materials (Basel) 12 (2019) 2967.
[30] M.M. Smith, Characterization of Linear Friction Welded In-Service Inconel 718 Superalloy, The University of British Columbia (Okanagan), 2017.
[31] K.R. VishwakAarma, O.A. Ojo, P. Wanjara, M.C. Chaturvedi, JOM 66 (2014) 2525–2534.
[32] T. Raza, K. Hurtig, G. Asala, J. Andersson, L.E. Svensson, O.A. Ojo, Metals (Basel) 9 (2019) 881.
[33] T. Raza, J. Andersson, L.-.E. Svensson, Sci. Technol. Weld. Joining 23 (2018) 606–611.
[34] F. Masoumi, D. Shahriari, M. Jahazi, J. Cormier, B.C.D. Flipo, Metall. Mater. Trans. A 48 (2017) 2886–2899.
[35] S. Tabaie, F. Rézaï-Aria, B.C.D. Flipo, M. Jahazi, Mater. Charact. 171 (2021) 110766.
[36] M. Cheepu, W.S. Che, Trans. Indian Inst. Met. 73 (2020) 1567–1571.
[37] P. Wanjara, J. Gholipour, K. Watanabe, K. Nezaki, Y. Tian, M. Brochu, Mater. Sci. Forum 879 (2016) 2072–2077.
[38] F. Masoumi, D. Shahriari, M. Jahazi, J. Cormier, A. Devaux, Sci. Rep. 6 (2016) 28650.
[39] F. Masoumi, M. Jahazi, D. Shahriari, J. Cormier, J. Alloys Compd. 658 (2016) 981–995.
[40] F. Masoumi, M. Jahazi, J. Cormier, D. Shahriari, MATEC Web of Conferences, EDP Sciences 2014 pp. 13005.
[41] S. Tabaie, F. Rézaï-Aria, M. Jahazi, Metals (Basel) 10 (2020) 587.
[42] N.E. Cowern, P.C. Zalm, P. van der Sluis, D.J. Gravesteijn, W.B. de Boer, Phys. Rev. Lett. 72 (1994) 2585–2588.
[43] K. Suzuki, H. Ito, T. Inoue, H. Miura, J. Solid Mech. Mater. Eng. 3 (2009) 487–497.
[44] P. Kringhøj, A.N. Larsen, S.Y. Shirayev, Phys. Rev. Lett. 76 (1996) 3372–3375.
[45] A. Chamanfar, M. Jahazi, J. Gholipour, P. Wanjara, S. Yue, Mater. Des. 36 (2012) 113–122.
[46] R. Giraud, Z. Hervier, J. Cormier, G. Saint-Martin, F. Hamon, X. Milhet, J. Mendez, Metall. Mater. Trans. A 44 (2012) 131–146.
[47] S. Ghorbanpour, M.E. Alam, N.C. Ferreri, A. Kumar, B.A. McWilliams, S.C. Vogel, J. Bicknell, I.J. Beyerlein, M. Knezevic, Int. J. Plast. 125 (2020) 63–79.
[48] M. Legros, G. Dehm, E. Arzt, T.J. Balk, Science 319 (2008) 1646–1649.
[49] O.T. Ola, O.A. Ojo, P. Wanjara, M.C. Chaturvedi, Metall. Mater. Trans. A 42 (2011) 3761–3777.
[50] W.M. Tucho, P. Cuvillier, A. Sjolyst-Kverneland, V. Hansen, Mater. Sci. Eng. A 689 (2017) 220–232.
[51] M.J. Sohrabi, H. Mirzadeh, Mater. Sci. Technol. 36 (2019) 380–384.
[52] O.T. Ola, O.A. Ojo, P. Wanjara, M.C. Chaturvedi, Metall. Mater. Trans. A 43 (2011) 921–933.
[53] O.A. Ojo, N.L. Richards, M.C. Chaturvedi, Scr. Mater. 50 (2004) 641–646.
[54] T.J. Ma, X. Chen, W.Y. Li, X.W. Yang, Y. Zhang, S.Q. Yang, Mater. Des. 89 (2016) 85–93.
[55] B. Gan, H. Murakami, R. Maass, L. Meza, J.R. Greer, T. Ohmura, S. Tin, Superalloys (2012) 83–91 2012.
[56] M. Pouranvari, J. Mater. Sci. Technol. 31 (2015) 1773–1780.
[57] S. Sui, H. Tan, J. Chen, C. Zhong, Z. Li, W. Fan, A. Gasser, W. Huang, Acta Mater 164 (2019) 413–427.
[58] Q. Li, X. Lin, X. Wang, H. Yang, M. Song, W. Huang, Metals (Basel) 6 (2016) 64.
[59] L. Heep, C. Schwalbe, C. Heinze, A. Dlouhy, C.M.F. Rae, G. Eggeler, Scr. Mater. 190 (2021) 121–125.
[60] M. Panella, L. Signor, J. Cormier, M. Bernacki, P. Villechaise, Superalloys 2020 (2020) 570–578.
[61] Y.-.S. Kong, M. Cheepu, D.-.G. Kim, Trans. Indian Inst. Met. 73 (2020) 1449–1453.
[62] F. Masoumi, L. Thébaud, D. Shahriari, M. Jahazi, J. Cormier, A. Devaux, B.C.D. Flipo, Mater. Sci. Eng. A 710 (2018) 214–226.
[63] M. Smith, L. Bichler, J. Gholipour, P. Wanjara, Int. J. Adv. Manuf. Technol. 90 (2017) 1931–1946.
[64] N. Hansen, Scr. Mater. 51 (2004) 801–806.
[65] L.S. Ling, Z. Yin, Z. Hu, J.H. Liang, Z.Y. Wang, J. Wang, B.D. Sun, Mater. (Basel) 13 (2019) 151.
[66] L. Thébaud, Etude Des Relations Entre Microstructure Et Propriétés Mécaniques Du Nouveau Superalliage Base Nickel AD730™, ISAE-ENSMA Ecole Nationale Supérieure de Mécanique et d'Aérotechique, Poitiers, 2017.
[67] Y.-.T. Chen, A.-.C. Yeh, M.-.Y. Li, S.-.M. Kuo, Mater. Des. 119 (2017) 235–243.
[68] Y. Xu, W. Li, X. Yang, Y. Gu, Mater. Sci. Eng. A 788 (2020) 139596.
[69] H. Yang, L. Zhu, R. Zhang, J. Zhou, Z. Sun, Int. J. Plast. 126 (2020) 102610.
[70] J.M. Zhang, Z.Y. Gao, J.Y. Zhuang, Z.Y. Zhong, Metall. Mater. Trans. A 30 (1999) 2701–2712.
[71] A. Devaux, A. Helstroffer, J. Cormier., P. Villechaise, J. Douin, M. Hantcherli, F. Pettinari-Sturmel, in: 8th International Symposium on Superalloy 718 and Derivatives, Pittsburgh, Pennsylvania, John Wiley and Sons Inc., 2014, pp. 521–535.
[72] M. Lachowicz, W. Dudziński, M. Podrez-Radziszewska, Mater. Charact. 59 (2008) 560–566.